Effect of magnesium concentration vs. pure water attack on the leaching kinetics and mechanical properties of low-carbon cementitious pastes

Charlotte Dewitte, Laurie Lacarrière, Mejdi Neji, Alexandra Bertron, Alexandre Dauzères

To cite this version:

Charlotte Dewitte, Laurie Lacarrière, Mejdi Neji, Alexandra Bertron, Alexandre Dauzères. Effect of magnesium concentration vs. pure water attack on the leaching kinetics and mechanical properties of low-carbon cementitious pastes. Cement and Concrete Composites, 2026, 169, pp.106518. ⟨10.1016/j.cemconcomp.2026.106518⟩. ⟨hal-05578099⟩

HAL Id: hal-05578099
https://hal.science/hal-05578099v1

Submitted on 2 Apr 2026

Cement and Concrete Composites 169 (2026) 106518

Contents lists available at ScienceDirect

Cement and Concrete Composites

journal homepage: www.elsevier.com/locate/cemconcomp

Effect of magnesium concentration vs. pure water attack on the leaching kinetics and mechanical properties of low-carbon cementitious pastes

Charlotte Dewitte [a,b,*], Laurie Lacarrière [b], Mejdi Neji [a], Alexandra Bertron [b], Alexandre Dauzères [a]

[a] Autorité de sûreté nucléaire et de radioprotection (ASNR), PSE-ENV/SPDR/LETIS, F-92260, Fontenay-aux-Roses, France
[b] Université de Toulouse, UPS, INSA, LMDC (Laboratoire Matériaux et Durabilité des Constructions), 135 Avenue de Rangueil, Cedex 04, 31077, Toulouse, France

ARTICLE INFO

Keywords:
Blended cement
Leaching
X-ray diffraction
EDS
Microstructure
Mechanical properties

ABSTRACT

With the increasing use of mineral additions to partially replace Portland cement, reaction mechanisms and the effects of chemical attack on material properties change. A recent study examined magnesium attack on a model low-carbon cementitious paste, but the influence of Mg concentration on the observed mechanisms remains unclear. To investigate this, a low-carbon model cementitious paste was exposed to 5 and 50 mmol/L $MgCl_2$ solutions for few months, as well as in pure water, to assess its impact on leaching kinetics and mechanical properties. The increase in $MgCl_2$ concentration, leads to a comparable phenomenology, only the deterioration rate increases with higher Mg levels. When immersed in pure water, the Ca leaching of the paste is more progressive, and the degraded depth is slightly lower than that of magnesium attack. Immersion in pure water appears to generate larger pores compared to magnesium attack and a higher reduction in E_{PSIM} is observed.

1. Introduction

In recent decades, a growing number of Supplementary Cementitious Materials (SCMs) have been developed and used in the construction of concrete civil engineering structures. This increasing use is justified by environmental considerations and efforts to improve physical, mechanical or setting properties for example ([1–6]). However, the use of mineral additions substituting part of Portland cement changes the mineralogical and chemical composition of cementitious materials. Thus, with the use of silica fume, slag and/or fly ash, the pH of the pore solution and the CaO/SiO_2 (C/S) atomic ratio of the hydrated material decrease. The amount of portlandite in hydrated binders decreases to zero when the C/S ratio of raw materials becomes very low ($C/S < 1.5$, [7–10]).

A magnesium attack on the concrete of infrastructures (ports, bridges, dams, nuclear waste repositories, etc.) can occur from contact with soft water ([11]), seawater ([12]) or clay poral water in the context of Cigeo ([13]). Cigeo is a French project to design and implement a possible deep geological repository for radioactive wastes in France. In the contact zones between the rock and the concrete, the use of low-pH (or low-C/S) concrete is foreseen in order to limit the disturbance of the concrete contact on the clay of the host rock and the swelling clay used to close the galleries ([14–16]). Portlandite plays an important role in magnesium attack. Its dissolution leads to the formation of a protective layer of brucite ([11,13,17]). In the absence of portlandite, the reaction mechanisms and the consequences of the chemical attack on the properties of the materials are expected to be different. For example [13], observed a much deeper magnesium enrichment in the cementitious paste in the case of a low C/S material compared to a Portland cement-based material (1.6 mm versus 10 μm). In order to better characterize and further predict the behaviour of low-C/S binders in these complex environments, understanding the mechanism of the different attacks is crucial. To estimate the durability of energy or safety related structures in these magnesium environments, the chemo-mechanical behaviour of low-pH (or low-C/S) materials subjected to magnesium attack needs to be characterized.

In engineering practice, the material in service is the concrete composite rather than the cement paste alone, and SCMs are commonly included. However, field investigations have consistently shown that chemical degradation in aggressive environments primarily affects the cement paste matrix, while aggregates remain largely inert [11,17,18]. For this reason, paste specimens are widely used as a model system to

---

* Corresponding author. Autorité de sûreté nucléaire et de radioprotection (ASNR), PSE-ENV/SPDR/LETIS, F-92260, Fontenay-aux-Roses, France.
E-mail addresses: charlotte.dewitte@emse.fr (C. Dewitte), laurie.lacarriere@insa-toulouse.fr (L. Lacarrière), mejdi.neji@asnr.fr (M. Neji), bertron@insa-toulouse.fr (A. Bertron), alexandre.dauzeres@asnr.fr (A. Dauzères).

https://doi.org/10.1016/j.cemconcomp.2026.106518
Received 6 August 2025; Received in revised form 12 January 2026; Accepted 7 February 2026

isolate and better understand the fundamental chemo-mechanical degradation mechanisms. In particular, low-C/S binders representative of SCM-rich concretes provide a relevant framework for investigating magnesium-induced degradation in low-carbon cementitious materials.

Recent studies have investigated the damage mechanisms in cement pastes exposed to $MgCl_2$ solutions, considering chemical, microstructural, and mechanical aspects [19–21]. However, these studies focused on Portland cement systems with high C/S ratios, where portlandite is present. Consequently, brucite formation occurs, and the degradation mechanisms are not expected to be comparable to those in pastes that do not contain portlandite. Several studies have investigated the impact of magnesium on low-carbon cement paste model systems [22–24]. Two studies focused on synthesized calcium silicate hydrate (C-S-H) and involved immersing the powders in a large volume (water/solid >50) of magnesium solutions ($MgCl_2$, MgO, or $MgSO_4$) [22,23]. These studies primarily examined the thermodynamic and mineralogical aspects of magnesium attack. Depending on the concentration, magnesium salts such as $MgCl_2$ or $MgSO_4$ can lower the pore solution pH and induce destabilization of C-S-H systems [22,23]. When exposed to 0.05 mol/L $MgCl_2$, the main hydrates identified were a mixture of magnesium silicate hydrate (M-S-H) and C-S-H. At the higher concentration of 0.5 mol/L Mg, however, M-S-H became predominant [22]. The Ca/Si and Mg/Si ratios in the hydrates increased with the initial Ca/Si ratio of the C-S-H, independently of the anion present in the solution. These phase assemblage results suggest that C-S-H with a lower Ca/Si ratio is less resistant to magnesium attack [22]. Conversely, the addition of MgO increases the pH and leads to the formation of brucite and M-S-H [23]. Since the materials were synthesized C-S-H, it was not possible to analyse the microstructural and mechanical properties resulting from this attack.

Our previous study investigated the effects of magnesium attack by exposing a low-carbon model paste (monolithic hydrate paste composed of low C/S C-S-H and ettringite) to a 5 mM $MgCl_2$ solution, representative of the clay poral water in the context of Cigeo [24]. A uniform enrichment in magnesium was observed (formation of M-S-H), as well as significant decalcification and dissolution of C-S-H. The mechanical properties within the Mg-enriched zone were significantly weaker than those of the unaltered material. This study provided insight into the degradation mechanisms associated with magnesium attack at intermediate Mg concentrations (5 mM), highlighting the resulting microstructural and mechanical changes. However, the magnesium concentration in natural environments varies widely, from 0.05 mM [11] to 50 mM [12]. It remains unclear whether higher magnesium concentrations, such as those found in natural environments could induce a change in degradation mechanisms, reaction products, or mechanical response. In particular, it is unknown whether increasing magnesium concentration leads to the formation of M-S-H with higher Mg/Si ratios, alternative Mg phases, or other mechanistic regimes, limiting our ability to generalize findings to environments such as seawater [12]. Additionally, the study revealed substantial calcium leaching alongside magnesium enrichment. Comparing these results to those from a pure water attack, often considered a reference in the field, could further clarify degradation processes.

The present study addresses this question by exposing a low-carbon model cement paste, mainly composed of C-S-H and free of portlandite (as is typical for low C/S binders) to 50 mmol/L $MgCl_2$ solution for up to 6 months, with additional experiments in pure water as reference. Data from these conditions are compared to our previous 5 mM $MgCl_2$ study [24], using the multi-technique characterisation developed by Dewitte et al. [24], combing elemental analysis by energy-dispersive spectroscopy (EDS), mineralogical composition determined by X-ray diffraction (XRD), microstructural analysis through microtomography and nitrogen physisorption, and evaluation of elastic properties using micro-indentation. The new magnesium concentration used in this study corresponds to that of seawater [12]. This multi-technique approach allows us to determine whether increasing Mg concentration alters the mechanisms of degradation or primarily accelerates known processes, and to compare the chemo-mechanical consequences of magnesium versus pure water attack. By explicitly examining these effects, this work clarifies the domain of validity of magnesium-controlled degradation mechanisms in low-carbon cementitious systems and provides new insights for durability assessment in Mg-rich environments such as seawater.

2. Materials and methods

2.1. Materials and sample preparation

A model cement paste was developed in a previous study in order to study the impact of magnesium attack on a simplified system [24]. According to TGA and XRD, this paste contains only C-S-H (without portlandite as is typically for low C/S cementitious pastes) and ettringite. The silica and calcium distribution is homogeneous in the material. The same model paste was used in this paper to understand the effect of magnesium on the leaching kinetics of low-carbon cementitious pastes. The model cement paste (referred to as CEMI-sil-col) was prepared using Portland cement (CEM I), colloidal silica, Milli-Q distilled water, and a superplasticizer. The colloidal silica used was Rheomac AS 150 (also marketed as Mastermatrix 150), supplied by BASF® as an aqueous suspension with a dry extract of 52 ± 2.5%. The Portland cement was a CEM I 52.5 N CE PM-ES-CP2 NF, sourced from Val d'Azergues (cement oxide composition is provided in Table 1). The superplasticizer was CHRYSO® Fluid Optima 175, provided by Chryso France®.

The pastes were produced using mechanical mixing at speeds ranging from 140 to 285 rpm for 8 min, powered by a 450 W mixer. The water-to-binder ratio (w/b) and superplasticizer dosage were adjusted to ensure adequate workability. The specific proportions are listed in Table 2.

Following casting, the pastes underwent 11 months of endogenous curing. Cuboidal specimens ($4 \times 4 \times 1$ cm^3) were subsequently prepared, and their 4×1 cm^2 lateral surfaces were covered with Resoltech® Mastic EPOXY 3030/3036 to induce controlled, unidirectional degradation.

2.2. Degradation procedure

Two types of aggressive solutions were tested in this study: an $MgCl_2$-based solution and pure water.

2.2.1. MgCl2 solution

The specimens were exposed to solutions containing $MgCl_2$ at concentrations of 5 and 50 mmol/L in sealed 60 L containers for periods of 2, 4 and 6 months. The solutions were continuously stirred and periodically renewed, with renewal times indicated by vertical dashed black lines in Fig. 1. The pH was measured in each tank before and after each renewal (Fig. 1). It can be observed that the pH increases as the $MgCl_2$ solution comes into contact with the model cementitious materials. During the test, under the effect of alkaline releases from the matrix, the attack solution thus has a pH close to 7. The results for the samples exposed to 5 mmol/L $MgCl_2$ have been previously published [24] and are indicated by an asterisk (*) in the following figures and referenced in the corresponding captions.

Samples were collected at 2, 4, and 6 months of exposure; they were then cut and prepared for the various characterization techniques.

2.2.2. Pure water

Two samples were immersed in a 3L Milli-Q water tank. The pH was maintained by a pH controller set to 7 using hydrochloric acid (HCl) diluted to 0.25 mol/L. As soon as the volume of acid added reached 30 mL, the 3L solution was renewed. In the test configurations, the ratio of solid surface area to solution volume is higher than in the $MgCl_2$ test, so contact of pure water with cementitious materials would quickly lead to

Table 1
Oxides proportion in CEM I 52,5 N CE PM-ES-CP2 NF (mass %).

Oxides	SiO_2	Al_2O_3	Fe_2O_3	CaO	MgO	K_2O	Na_2O	SO_3	TiO_2	MnO	P_2O_5	CO_2
Proportion (%)	20.6	3.60	5.00	64.3	0.70	0.70	0.20	2.70	ND	ND	0.40	0.90

Table 2
Mix proportions for the CEMI-sil-col cement paste.

CEM I (g)	Rhéomac AS 150 (g)	MilliQ-water (g)	Superplasticizer (dry extract) (g)	Sp/b	w/b
590.5	621.7	275.1	10.56	1.20%	0.65

Sp/b: mass ratio of superplasticizer to binder; w/b: mass ratio of water to binder.

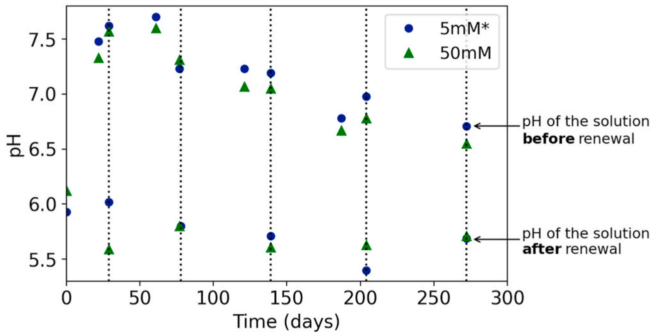

Fig. 1. pH evolution of the 60L $MgCl_2$ solutions (5 mmol/L [24] and 50 mmol/L) over time.

significant pH rises. In order to maintain pH conditions close to those of the $MgCl_2$ test (for which the pH was observed to be close to 7, except at the time of renewal when it momentarily dropped to around 6), the pH is controlled during the leaching test by adding HCl. The pH and HCl volume added were measured continuously (Fig. 2).

2.3. *Multi-technique characterization*

The degraded materials studied exhibit gradients in chemical, microstructural, and mechanical properties. To better characterize these gradients and correlate various analyses, a methodology developed in a previous study [24] is applied in this work. Selected datasets from our previous study [24] are reproduced in this manuscript solely for comparison purposes and are systematically cited throughout the text and in all corresponding figure captions. More than two-thirds of the experimental data presented here are new, including all results obtained at 50 mM $MgCl_2$, the complete set of pure water experiments, and the associated microstructural and mechanical analyses.

2.3.1. *Sample preparation*

Chemical analyses using energy-dispersive X-ray spectroscopy (EDS) and indentation measurements were performed on flat, polished cross-sections of the samples. The polishing protocol is detailed in Table 3. Each step was followed by rinsing the sections with ethanol. The retention strength was 30 N and the rotation speed was 250 rd/min. The abrasive product was SiC. All polishing consumables were obtained from Struers©, and polishing was conducted using a Struers LaboPol-2© system.

Assessing microstructural alterations induced by degradation through N_2 physisorption required collecting a significant quantity of material representative of the degraded area. Following degradation, the sound and degraded zones were separated to obtain distinct samples from each region. To minimize cross-contamination, the interface was polished. To ensure accurate porosity determination by nitrogen physisorption, the pore water was removed. The specimens were cut into pieces of roughly 0.2 cm^3, subjected to freeze-drying under nitrogen, and maintained in a Crios-50 (Cryotec) freeze dryer for at least five days prior to measurement.

Approximately 100 mm^3 portions of the degraded material were taken for X-ray microtomography and sealed under parafilm immediately at the tank exit to preserve their state. For the XRD analysis, after cutting a portion of the sample, an initial measurement was performed on the surface that had been in direct contact with the aggressive solution. Subsequently, the surface was manually abraded using 800-grit abrasive paper. The depth of abrasion at each stage was recorded with a digital gauge accurate to 0.001 mm, at a single point. Due to the manual nature of this procedure, these values provide only an approximate indication of the true abrasion depth. It should be noted that the amorphous phases (C-S-H and M-S-H) are not quantitatively determined in this study. Techniques suitable for amorphous phase quantification (e.g., TGA or ^{29}Si NMR) require large amounts of powdered material, which is incompatible with the spatially resolved characterization performed on solid cross-sections.

Table 3
Polishing protocol for cement paste specimens for indentation and SEM.

Step	1	2	3	4	5
Abrasive Paper (Grit Number)	500	800	1200	2000	4000
Lubricant	Ethanol	Ethanol	Ethanol	Ethanol	DP-Lubricant Brown
Time	2–4 min	30 s	1 min	1 min 30 s	6-8 min

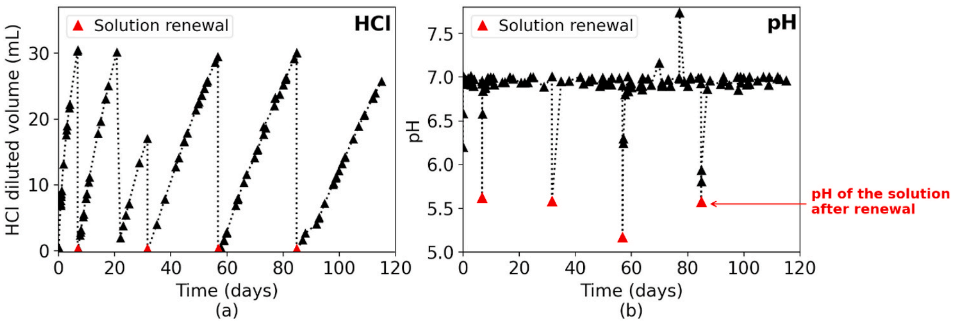

(a)

(b)

Fig. 2. HCl volume injected (a) and pH (b) evolution over time in the pure water attack (0 mM).

2.3.2. *Mineralogical and chemical analyses*

X-ray diffraction (XRD) analyses were performed using a Malvern Panalytical Aeris diffractometer operating at 600 W, 40 kV, and 15 mA, equipped with a Cu anticathode ($\lambda \approx 1.54$ Å). Measurements were conducted on powder samples (sound material) and solid samples (degraded material). For the sound samples and the surface and sound zones of the degraded samples, scans were performed over a 2Θ range of 5° to 70° with a step size of 0.0109°, resulting in a total acquisition time of 1 h. Due to crack formation, analysis times for other abrasion depths of the degraded samples were reduced to 20 min. Diffractograms were plotted as intensity versus 2Θ angle, denoted [2Θ] CuKα.

Solid chemical characterization was performed using an energy-dispersive spectrometer (EDS) coupled to a scanning electron microscope (SEM, Hitachi S3500N), equipped with two Bruker 5030 XFlash detectors operating at 15 kV. Elemental maps were acquired by collecting hyperspectral images over an area of 1536 × 1152 μm^2, with a 3 μm spatial resolution, with an acquisition time of 1 h and 47 min. EDS elemental mapping was performed on selected regions close to the exposed surface in order to characterize the altered zones. Mapping of the full sample thickness was not carried out because of the very long acquisition time (≈1 h 45 per 1.5 × 1.1 mm^2 area, to allow 3 μm resolution with high signal at each point and low noise) and the fact that the sound core of the specimens was shown to be compositionally homogeneous.

2.3.3. *Microstructural analyses*

Nitrogen adsorption–desorption isotherms were acquired using a Micromeritics 3Flex instrument (MIC271002 REV B) with 3Flex software version 4.05. Prior to measurement, the freeze-dried samples were degassed in the sample cell under vacuum at 45 °C for 4 h to eliminate water and other physically adsorbed volatiles. Adsorption and desorption measurements were then performed over a period of about 20 h. The specific surface-area ($SSA_{B.E.T}$) was calculated using the Brunauer–Emmett–Teller (BET) equation [25] within the relative pressure range of 0.05–0.2. Pore size distributions were determined using the Barrett–Joyner–Halenda (BJH) method [26], and pore volumes for pores between 2.5 and 10 nm were obtained from the t-curve (derived from Aerosil 200 as in Ref. [27]) for $p/p^0 < 0.8$, using the second slope in the 7–10 Å range [27–29].

Tomographic imaging of the samples was carried out with a SkyScan 1272 system (Bruker micro CT N.V., Fontenay-aux-Roses). To preserve their condition, all specimens were sealed with parafilm prior to and during scanning. The X-ray source operated at 100 kV and 100 mA, providing sufficient contrast between phases and pore spaces. Radiographs were collected at 0.1° rotation increments, resulting in an acquisition period of approximately 20 h. The reconstructed images achieved a spatial resolution of 2 μm.

2.3.4. *Elastic properties characterizations*

To assess the elastic properties at the mesoscale, local microindentation tests were conducted on samples immersed in 5 mM $MgCl_2$ for 6 months, 50 mM $MgCl_2$ for 4 and 6 months, and in pure water for 4 months. The effect of degradation on the Poisson's ratio is unknown, which makes it impossible to directly determine the elastic modulus from indentation tests. The evolution of elastic properties is therefore assessed using the plane strain indentation modulus (E_{PSIM}). The calculation of this modulus follows:

$$E_{PSIM} = \frac{E_{IT}}{(1-\nu^2)} = \frac{E_r * E_i}{E_i - E_r * (1-\nu_i{}^2)} \tag{1}$$

where E_{PSIM} is the plane strain indentation modulus, E_{IT} and ν denote respectively the elastic modulus and the Poisson's ratio of the tested material, while E_i and ν_i correspond to the elastic modulus and the Poisson's ratio of the indenter.

Indentation tests were performed on polished sections of the cementitious samples, using a nanoindenter (NHT^3, Anton Paar ®) equipped with a Berkovich tip, following the same polishing procedure as for SEM/EDS (see Table 3). Microindentation was performed under force control with a maximum load of 200 mN, applied at a rate of 100 mN/min, followed by a 10-s pause at maximum load, and an unloading rate of 100 mN/min. Indents were spaced 300 μm apart to prevent interaction between neighboring points ($\Delta > 30*h_{max}$) [30]. Multiple grids of 4 × 4 indents were performed from the left exposed surface ($z = 0$) to the right exposed surface. Between 4 and 7 lines were produced per sample, and values were averaged by column (for each z-position) to generate a one-dimensional elastic property profile (see Ref. [24] for further details on the method). Since the same polished sections were used for both microindentation and SEM/EDS analyses, a thin carbon layer (~300 Å) was present on the sample surface. This layer thickness is considered negligible, as indentation depths ranged between 5 and 10 μm.

3. Results

3.1. *Mineralogical and chemical characterisation*

SEM/EDS analyses were conducted after 4 months of exposure to the aggressive solutions to visualise the degradation front and characterize the chemical evolution in the degraded samples. Based on the magnesium, calcium, and silicon EDS maps, Ca/Si and Mg/Si intensity ratio profiles were calculated by averaging the elemental intensity ratios across pixel columns. To minimize the influence of holes and cracks (approximately 2000–2300 μm for 50 mM), Mg/Si and Ca/Si values outside the range [0, 3] were excluded. Fig. 3 presents the Ca/Si intensity ratio profiles together with cropped sections of the corresponding calcium EDS maps, showing only a thin representative layer above the profiles. These sections are representative of the overall microstructure, as the degradation fronts are homogeneous. Full, uncropped EDS maps are provided in the supplementary data (Fig. 13). The surfaces facing the solutions are on the left side of each map ($x = 0$).

An analogous figure based on magnesium rather than calcium is presented in Fig. 4.

In both cases, with or without magnesium in the attack solution, calcium leaching is observed. However, in the presence of magnesium, the Ca-leached zone exhibits magnesium enrichment. This leaching process is notably more pronounced when magnesium is present in the attack solution. The profiles are similar to those observed in electron probe microanalysis (EPMA), as seen in the previous study with the 5 mM aggressive solution [24].

The two figures display distinct zones: a sound zone, a transition zone characterized by a progressive decrease in the Ca/Si ratio, and, in Mg-attacked samples, a highly decalcified zone in which the Ca/Si ratio reaches a stable and low value. Table 4 presents the depths corresponding to these zones for the three samples.

Increasing the magnesium concentration in the aggressive solution does not change the degradation pattern. Both pastes subjected to magnesium attack, at either 5 mM or 50 mM $MgCl_2$, show the same three zones. The only difference is that the degraded depth increases with the magnesium concentration. The Mg/Si intensity ratio remains stable in the highly decalcified zone (Zone 3 in Table 4), with a localized Mg/Si increase near the surface, indicating that the Mg concentration does not affect the chemistry of the degraded zone.

When the samples are immersed in pure water, the apparent depth of degradation is comparable to that observed with magnesium exposure at 5 mM $MgCl_2$ (Figs. 3 and 4). Examining the Ca/Si profiles (Fig. 3), for pure water, the Ca/Si (Intensity) decreases more rapidly under magnesium attack than in pure water attack, suggesting a more gradual destabilization of the C-S-H phase when in contact with pure water only. Moreover, the two pastes subjected to magnesium attack, either at 5 mM or 50 mM $MgCl_2$, show a zone where the Ca signal is very weak (Zone 3 in Table 4). No such zone is observed for the sample immersed in pure

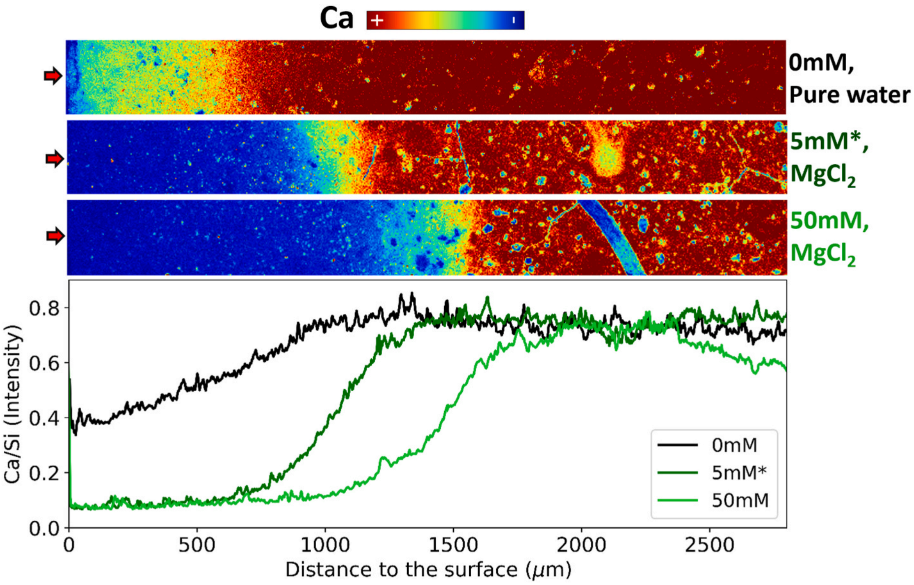

Fig. 3. Calcium distribution and Ca/Si ratios in low-pH cement paste after 4 months of exposure in pure water (0 mM), 5 mM $MgCl_2$ [24], or 50 mM $MgCl_2$ solutions.

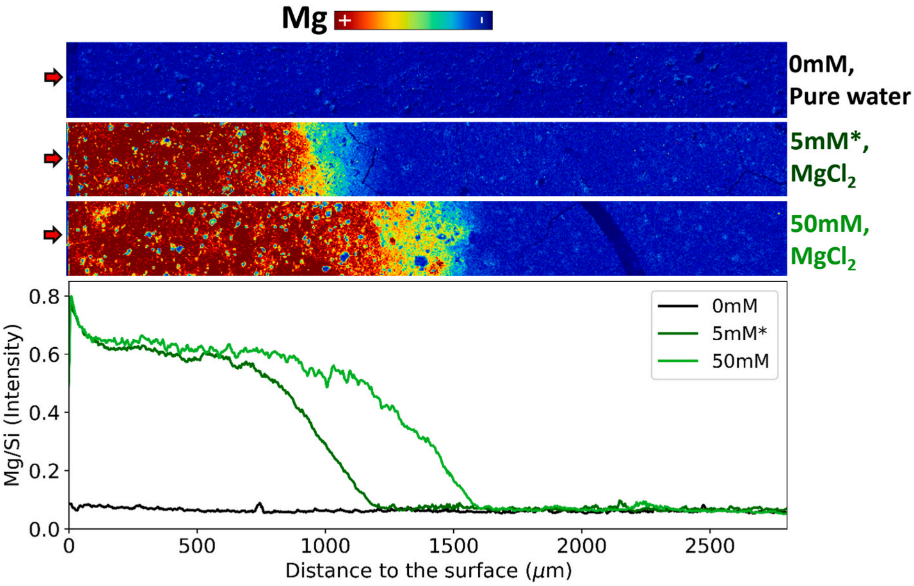

Fig. 4. Magnesium distribution and Mg/Si ratios in low-pH cement paste after 4 months of exposure in pure water (0 mM), 5 mM $MgCl_2$ [24], or 50 mM $MgCl_2$ solutions.

Table 4
Position of zones in a low-pH cement paste after 4 months of exposure in pure water (0 mM), 5 mM $MgCl_2$ [24] or 50 mM $MgCl_2$ solutions.

	Pure water	5 mM $MgCl_2$ *	50 mM $MgCl_2$
Zone 1: Sound zone	>1000 µm	>1250 µm	>1600 µm
Zone 2: Transition zone	<1000 µm	[750, 1250] µm	[1100, 1600] µm
Zone 3: Highly decalcified zone	Not observable	<750 µm	<1100 µm

water (0 mM). Consequently, no fully degraded zone is observed in the sample exposed to pure water, implying that complete decalcification may not yet have occurred, as Ca degradation progresses more slowly.

The mineralogical composition of the pastes as a function of the distance from the surface exposed to pure water and $MgCl_2$ solutions for 4 months was characterized by XRD. For each sample, three representative diffractograms were selected and are presented in Fig. 5, corresponding to the previously defined zones: the sound zone (zone 1, (a)), the transition zone (zone 2, (b)), and the highly decalcified zone (zone 3, (c)). For zone 3, the diffractograms correspond to measurements acquired directly at the exposed surface. For the transition zone, the depths at which the diffractograms were acquired are indicated in the figure above the concentration labels: 290 µm for 0 mM, 405 µm for 5 mM, and 605 µm for 50 mM. These depths were estimated from manual abrasion steps and should therefore be regarded as approximate; the EDS profiles shown in Figs. 3 and 4 should be taken as the reference for locating the transition zone. The complete set of diffractograms, together with the corresponding calcium EDS maps, is provided in the supplementary data (Fig. 14). In addition, all XRD patterns obtained for the 50 mM samples at 2, 4 and 6 months are presented in the supplementary data (Fig. 15) to

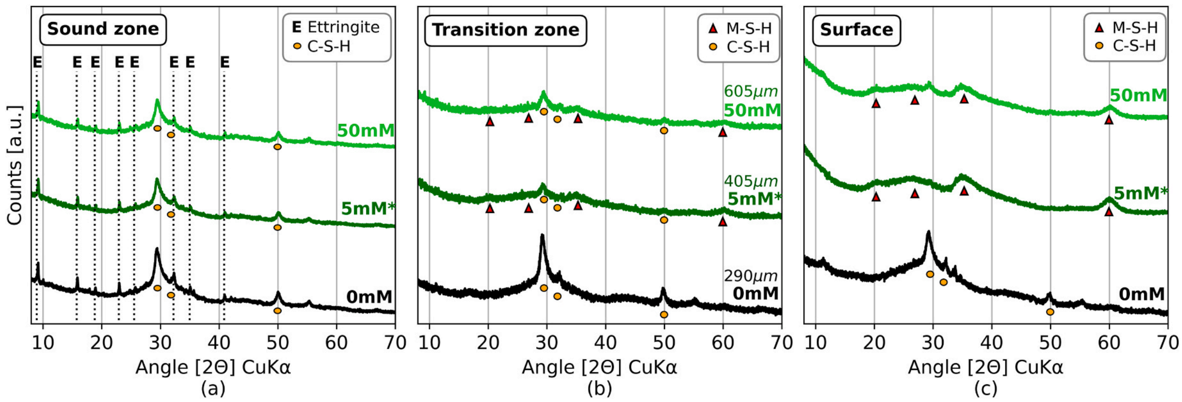

(a) (b) (c)

Fig. 5. X-ray diffractograms of a low-pH cement paste after 4 months in pure water (0 mM), 5 mM $MgCl_2$ [24], or 50 mM $MgCl_2$ solutions, shown for (a) the sound zone, (b) the transition zone, and (c) the highly decalcified zone (surface).

support the discussion of concentration effects.

In the transition zone of the sample immersed in pure water, C-S-H was detected. A hump around 30 [2θ] CuKα increases in size as it approaches the surface and could correspond to silica gel. However, its amorphous nature complicates the identification of its presence through XRD analysis. Similar diffractograms were observed by Swanton et al. [31] in Ca-Si systems with a C/S ratio of around 0.4 indicating the presence of C-S-H and silica gel. Furthermore, at such a low pH (7), silica gel is more stable than C-S-H [32,33]. Thus, the C-S-H gradually decalcifies and forms silica gel.

For samples exposed to magnesium attack, the transition zone contained a mixture of C-S-H and M-S-H. In the highly decalcified zone, observed only in pastes exposed to magnesium attack, M-S-H was exclusively identified in both cases. In a previous study on samples exposed to a 5 mM $MgCl_2$ solution for six months [24], stoichiometric balance calculations, supported by quantitative microprobe analyses, revealed that the degraded zone also contained silica gel. It is likely that amorphous silica is similarly formed in the degraded zone of the present pastes.

3.2. Microstructure

To observe the microstructure changes, microtomography mappings were performed. Unfortunately, it was not feasible to conduct these measurements at identical degradation times for all samples. Nevertheless, the results provide valuable insights into density changes along the degradation profile. Fig. 6 displays the normalized density profiles derived from these microtomography mappings. For the 50 mM sample, the surface was slightly skewed and the microtomography planes for z < 800 μm include voids. As a result, these data are not considered and are not plotted.

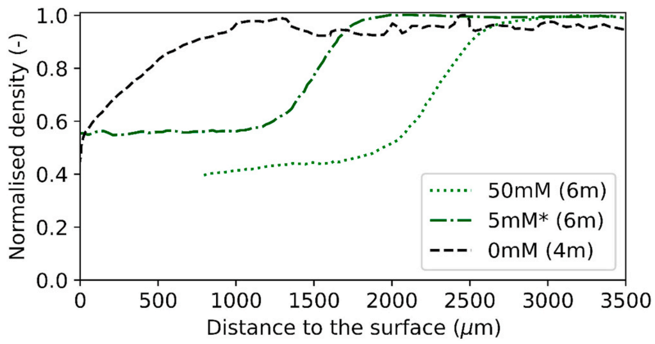

Fig. 6. Normalized density profiles from microtomography of low-pH cement paste after 4 months in pure water (0 mM) and 6 months in 5 mM $MgCl_2$ [24] or 50 mM $MgCl_2$ solutions.

A similar density profile is observed for both pastes subjected to magnesium attack, with density profiles corresponding to the decrease in the Ca/Si ratio (Fig. 3). The primary difference lies in the normalized density values within the degraded zone, which are slightly lower for the sample with the higher Mg concentration ($\rho_{deg}/\rho_{sound} = 0.55$ for 5 mM and 0.45 for 50 mM). EDS analyses (Figs. 3 and 4) indicate that both samples exhibit the same chemical composition in this region. Thus, this difference may be attributed to either (i) increased porosity in the 50 mM sample or (ii) measurement variability.

For the sample subjected to pure water attack, a similar density profile is observed, mirroring the previously presented Ca/Si profile (Fig. 3). In the degraded zone, the density decreases by 50%, with the remaining Ca/Si intensity measured at 0.4 (Fig. 4). Therefore, despite the persistence of calcium, the surface density reaches a comparable value in samples exposed to both pure water and magnesium attacks.

The microstructure of the degraded zone (Z2-Z3 as defined previously) and sound zone (Z1) was studied by N_2 Physisorption (Fig. 7 and Table 5). The isotherm, pore size distribution (BJH) and specific surface area of the sound zone for the three degraded samples were similar (Average Specific Surface B.E.T $= 47.0 \pm 5.8$ (m^2/g)). Thus, only one is displayed in Fig. 7 and the average value is shown in Table 5.

The isotherms (Fig. 7a) and pore size distributions (Fig. 7b) are similar for the two pastes immersed in 5 and 50 mmol/L $MgCl_2$, indicating no significant difference in microstructure with increased Mg concentration in the aggressive solution. Additionally, Mg degradation does not impact the intermediate pores (4 nm < d < 8 nm), as the isotherms (Fig. 7a) and BJH pore size distributions (Fig. 7b) are consistent between the sound and degraded zones in the samples exposed to magnesium attack. However, the degraded zones contain a higher quantity of small pores (d < 4 nm) than the sound zones in these samples. As noted in a previous study [24], this increase is consistent with the formation of M-S-H phases, which appear to possess high intrinsic porosity. Specifically, at the small scale ($p/p_0 < 0.4$) (Fig. 7a), the degraded zone exhibits properties similar to M-S-H pastes, including comparable specific surface area and an initial isotherm curve shape.

The degraded zone of the paste immersed in pure water exhibits a higher specific surface area compared to the sound zone (Table 5), although it is lower than that of the degraded zones exposed to 5 mM and 50 mM $MgCl_2$. For $p/p_0 > 0.4$ (Fig. 7a), the amount adsorbed is significantly higher in the pure water attack than in the magnesium attacks, indicating a larger quantity of larger pores. This observation is consistent with the BJH pore distribution (Fig. 7b), where an initial peak appears around 3.8 nm, similar to the degraded samples exposed to 5 mM and 50 mM $MgCl_2$, followed by a consistently higher curve in the upper pore range for the pure water-immersed sample. Thus, pure leaching appears to generate larger pores in the degraded zone compared to magnesium attack.

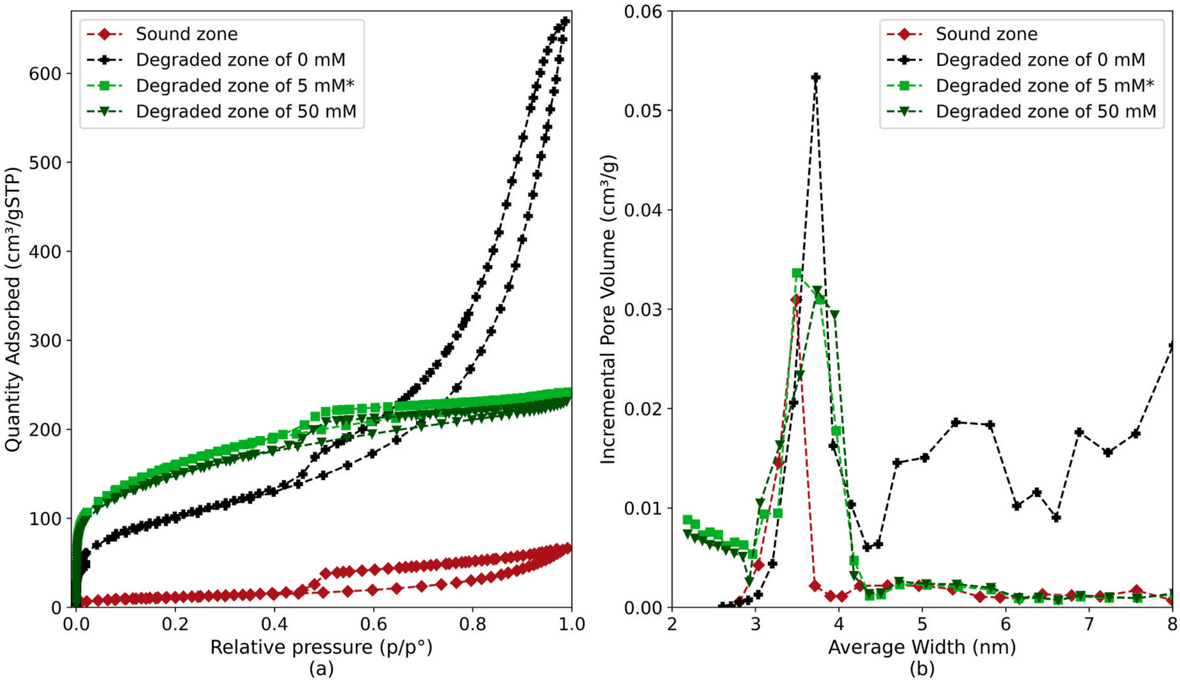

Fig. 7. **(a) N_2 adsorption-desorption isotherms and (b) Associated pore size distributions (BJH) of the sound zone and degraded zones of the samples immersed for 4 months in pure water (0m), 6 months in 50 mM $MgCl_2$ and 8 months in 5 mM $MgCl_2$** [24].

Table 5
Average BET specific surface area (m^2/g) of low-pH cement paste after 4 months in pure water or in $MgCl_2$ solutions at 5 mM [24] **and 50 mM.**

Aggressive solution	-	Pure water	5 mM $MgCl_2$	50 mM $MgCl_2$
Zone	Z1	Z2	Z2-Z3	Z2-Z3
Average Specific Surface B.E.T (m^2/g)	47.0	362.8	571.1	532.1

3.3. *Elastic properties*

The influence of mineralogical and microstructural changes on elastic properties was investigated by measuring the plane strain indentation modulus (E_{PSIM}) as a function of depth from the surface, using microindentation techniques. The results are presented for three cases of material degradation. Fig. 8 show E_{PSIM} measurements for model paste samples immersed for six months in 5 mM (adapted from Ref. [24]) and 50 mM $MgCl_2$ solutions. Fig. 9 illustrates the results for a model paste sample immersed for four months in pure water.

For pastes immersed in $MgCl_2$ solutions, the strong cracking that occurs between the sound and degraded zones makes indentation difficult or impossible. These zones are illustrated by the grey rectangles in Fig. 8. As in the study by Dewitte et al., 2024 [24], when the number of points per abscissa is less than 5, the value is excluded.

The evolution of elastic properties along the samples immersed in 5 mM and 50 mM $MgCl_2$ solutions shows a similar trend (Fig. 8). Characterizing the transition zone proved challenging due to significant microcracking, making data acquisition difficult in these areas, which are highlighted in grey in Fig. 8. Data are only reported for locations where at least five valid measurements (based on correct indentation curves) were obtained; otherwise, no data are displayed. In the 50 mM sample, substantial cracking in certain regions prevented successful data collection. Highly decalcified regions (Zone Z3, see Table 4) exhibit stable elastic properties around 2-5 GPa, indicating a 67–82% reduction in E_{PSIM}.

The sample immersed in pure water for four months (Fig. 9) also exhibited a reduction in the plane strain indentation modulus (E_{PSIM}). The results in this case are more reliable due to the higher number of data points obtained, as the material experienced less microcracking. As previously discussed, complete decalcification may not have occurred; however, E_{PSIM} is already considerably low (2 GPa, i.e. 15% of the sound zone) even though the calcium-to-silicon (C/S) ratio remains at 0.4.

4. Discussion

Additional EDS analyses were conducted on samples immersed in $MgCl_2$ solutions for 2 and 6 months. The results are provided in the supplementary data (Fig. 16) and a summary of the findings is presented in Figs. 10 and 11. These results confirm previous observations and illustrate the degradation profiles over time and across different concentrations.

The slope of the C/S = f(z) curve in zone 2 remains relatively constant (ranging from 8.5e-4 to 10.5e-4 μm^{-1}) for both magnesium concentrations (5 mM and 50 mM) and across all degradation times (Fig. 10 (b and c)). Therefore, increasing the Mg concentration does not seem to significantly alter the transition zone (Z2). In the case of pure water, the Ca/Si (Intensity) decreases linearly to approximately 0.4 with a slope of 3.7e-4 μm^{-1}. This lower slope indicates a more gradual decalcification when Mg is absent in the aggressive solution.

An increase in Mg concentration results in a greater degraded depth, as shown in Figs. 10 and 11. After four months of immersion in aggressive solutions, the degraded depth increased from 1000 μm in pure water to 1250 μm and 1600 μm in 5 mM and 50 mM $MgCl_2$ solutions, respectively. Magnesium acts as a calcium pump, with the Mg-Cl_2 complex replaced by the Ca-Cl_2 complex in solution. Henocq [34] demonstrated that C-S-H equilibrates at higher calcium concentrations in the presence of chloride ions. A comparison of our case studies—pure water and a 50 mM $MgCl_2$ solution—with Henocq's case studies of $CaCl_2$ 0 mM and $CaCl_2$ 50 mM reveals a clear trend: increasing $CaCl_2$ concentration results in higher calcium equilibrium concentration. In the absence of calcium in the aggressive solutions, the dissolution of C-S-H is required to establish equilibrium concentrations in the presence of chloride ions. Moreover, an increase in the magnesium content of the

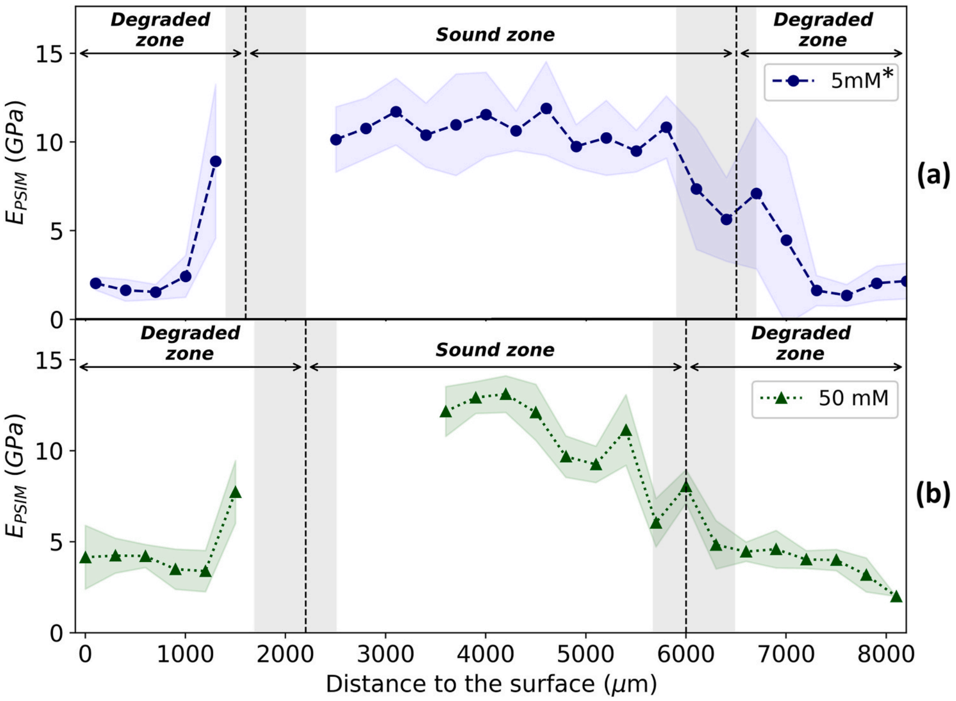

Fig. 8. 1D profile of the plane strain indentation modulus excluding outliers, for the model cement paste immersed (a) for 6 months in 5 mM of $MgCl_2$ (adapted from Ref. [24]**) and (b) for 6 months in 50 mM of $MgCl_2$. The grey rectangles correspond to the areas where micro-cracking was observed.**

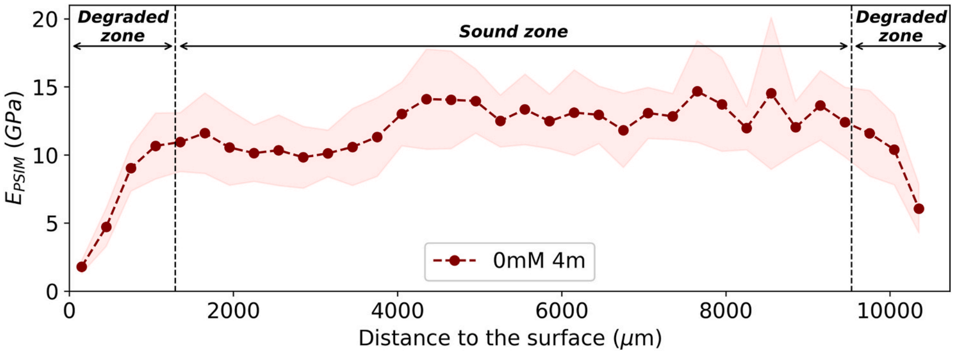

Fig. 9. 1D profile of the plane strain indentation modulus excluding outliers, for the model cement paste immersed for 4 months in pure water.

aggressive solution accelerates the decalcification of C-S-H. Additionally, an increase in the calcium concentration in the equilibrium solution enhances the concentration gradient, thereby promoting the outward diffusion of calcium.

Fig. 11 shows that the difference in degraded depth between 5 mM and 50 mM $MgCl_2$ solutions increases over time. The degradation front depth for the 50 mM samples is 1 to 1.4 times greater than that of the 5 mM samples. The relationship between degraded depth (Z1) and the square root of time ($\sqrt{t}$) (Fig. 11 (a)) exhibits a linear trend in both cases, indicating that the kinetics of magnesium attack on the cement paste is diffusion-controlled and can be described by Fick's law. The trend line for the 50 mM solution has a steeper slope (450 μm/months, with $R^2 = 0.99$) compared to the 5 mM solution (275 μm/months, with $R^2 = 0.99$), which is consistent with the earlier discussion on the effect of increasing Mg concentration on the calcium concentration in solution and the dissolution of C-S-H. Despite a tenfold increase in Mg concentration, no concentration-induced transition in degradation mechanisms or reaction products is observed; the primary effect of higher Mg levels is an acceleration of degradation kinetics rather than a change in the degradation regime.

To evaluate the effects of degradation on mechanical and microstructural properties, the calcium-to-silicon (C/S) ratio, which reflects the dissolution of C-S-H, was selected as the degradation indicator. The plane strain elastic modulus (E_{PSIM}) and normalized density were plotted as functions of this indicator (Fig. 12). In C-S-H with a low C/S ratio, such as in the sound cement paste, calcium loss leads to the dissolution of C-S-H and the formation of silica gel (in pure water) or M-S-H (in $MgCl_2$ solution). Notably, C-S-H becomes unstable when the C/S ratios drops below 0.7 [35]. A C/S ratio of 0.35 signifies that approximately half of the C-S-H has dissolved, promoting the formation of either silica gel or M-S-H, depending on the aggressive solution.

For C/S ratios greater than 0.5 (indicating that approximately 70% of the C-S-H remains), both types of aggressive solutions—pure water and $MgCl_2$ solution—exhibit a similar effect: a moderate reduction in density and modulus of elasticity. However, when the C/S ratio falls below 0.5, the two solutions exhibit distinct behaviors.

- In samples immersed in pure water (0 mM), there is a sharp decrease in both modulus and density. This suggests a loss of cohesion, as the C-S-H matrix no longer functions as a cohesive network (i.e., when more than 50% of it has dissolved) and the resulting silica gel provides minimal cohesion. This phenomenon has already been

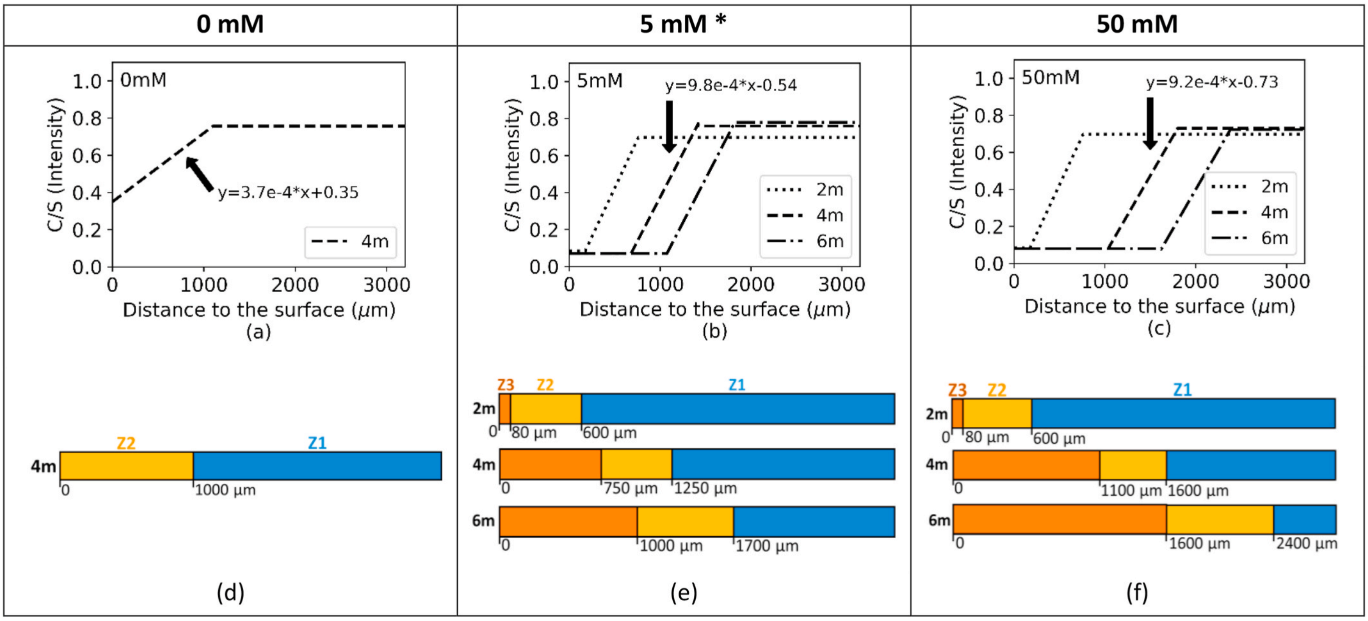

Fig. 10. **Schematic diagram of the evolution of the C/S ratio along the degradation (a, b and c) and the evolution of the zones with time (d, e and f) for the model cement paste immersed in pure water, 5 mmol/L $MgCl_2$ solution [24] and 50 mmol/L $MgCl_2$ solution respectively.**

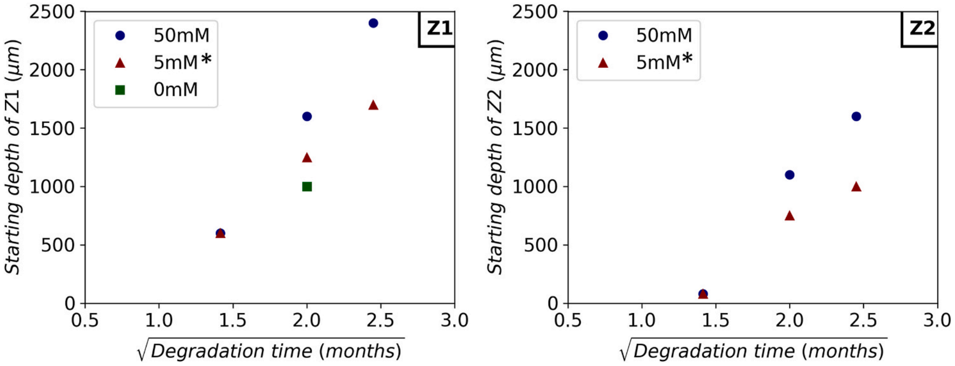

Fig. 11. Illustration of the limit of Z1 (a) and Z2 (b) in Fig. 10 plotted against the square root of the degradation time (in months).

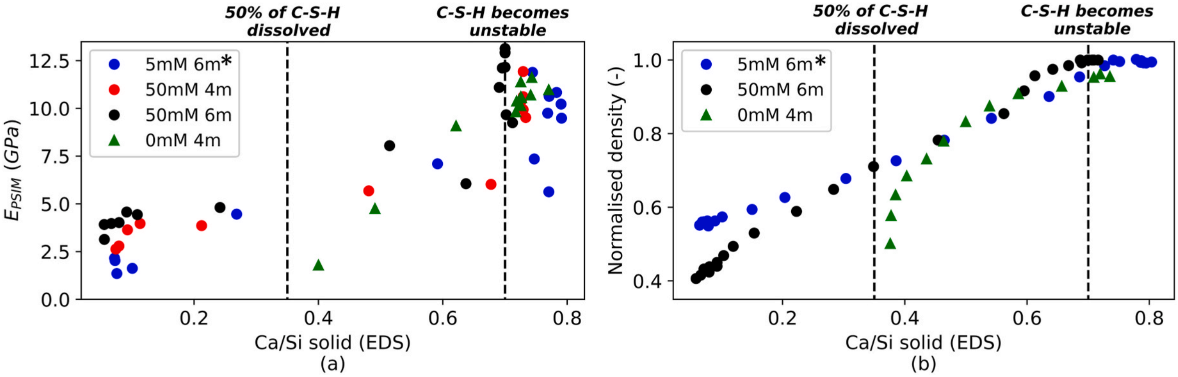

Fig. 12. **Plane strain elastic modulus (E_{PSIM}) and normalized density (calculated from microtomography) plotted as a function of Ca/Si solid (calculated from EDS maps) for the samples immersed in 5 mM $MgCl_2$ solution for 6 months [24], 50 mM $MgCl_2$ solution for 4 and 6 months, and in pure water for 4 months.**

observed by Carde [36], Gallé et al. [37] and Consantinides & Ulm [38] and has been modeled by Stora et al. [39].

- In samples immersed in $MgCl_2$ solutions, the loss of density is comparatively moderate. M-S-H, being denser than silica gel, appears to maintain the modulus at approximately 40% of its initial value, compared to 20% in the case of pure water.

5. Conclusion

This study aimed to investigate the effect of magnesium on the leaching kinetics and mechanical properties of low-carbon cementitious pastes. Model low-carbon cementitious pastes were immersed in aggressive solutions containing different magnesium concentrations of 0 mM (pure water), 5 mM $MgCl_2$, and 50 mM $MgCl_2$ for durations ranging from 2 to 6 months.

The increase of $MgCl_2$ concentration, from 5 mM to 50 mM, in the solution leads to a comparable phenomenology. A similar gradient of chemical concentrations was observed through EDS analysis. The contact of the sample with a 5 mM or 50 mM solution of $MgCl_2$ led to a strong enrichment in magnesium accompanied by calcium and sulfur leaching. The difference is the deterioration rate, which accelerates with higher Mg concentration. Despite this, the dissolved phases are identical and the Mg-attack leads to the formation of M-S-H at both concentrations. The M-S-H formed displays a similar microstructure as confirmed by N_2 Physisorption, to that observed in samples immersed in 5 mM of $MgCl_2$ [24]. Microtomography measurements also reveals an equivalent loss of density (approximately 50%) in the degraded zones for both concentrations. Likewise, indentation tests indicate a comparable reduction in the elastic modulus (around 80%) in the highly degraded zones for both pastes.

When the same paste is immersed in pure water, a more progressive Ca leaching from the core of the material to the surface happens. The degraded depth is slightly lower than that observed under magnesium attack with 5 mM MgCl2 and significantly lower than that under magnesium attack with 50 mM MgCl2. Unlike the case of magnesium attack, no completely degraded zone is observed, likely because the degradation process had not yet reached completion after 4 months of immersion. Magnesium functions as a calcium pump, facilitating ion exchange where the Mg-Cl_2 complex is progressively replaced by the Ca-Cl_2 complex in the solution. An increase in the magnesium concentration within the aggressive solution accelerates the decalcification of C-S-H. According to N_2 physisorption, immersion in pure water tends to generate larger pores in the degraded zone compared to samples subjected to magnesium attack. Finally, indentation tests revealed a significant reduction in E_{PSIM}, with values decreasing to 2 GPa (i.e. 15% of the sound zone).

A central outcome of this study is the demonstration that increasing magnesium concentration over an order of magnitude does not induce a transition in degradation mechanisms, reaction products, microstructure, or mechanical response. This result defines the domain of validity of magnesium-controlled degradation mechanisms in low-carbon cementitious systems. Furthermore, the comparison with pure water leaching highlights that chemical severity cannot be inferred solely from surface degradation or calcium loss, as distinct microstructural and mechanical responses are observed. Further investigations are necessary to understand the structural implications, potentially through finite element modeling or similar approaches.

CRediT authorship contribution statement

Charlotte Dewitte: Writing – review & editing, Writing – original draft, Visualization, Validation, Methodology, Investigation, Conceptualization. **Laurie Lacarrière:** Writing – review & editing, Validation, Supervision, Resources, Project administration, Methodology, Funding acquisition, Conceptualization. **Mejdi Neji:** Writing – review & editing, Validation, Supervision, Resources, Methodology, Conceptualization. **Alexandra Bertron:** Writing – review & editing, Validation, Supervision, Resources, Methodology, Conceptualization. **Alexandre Dauzères:** Writing – review & editing, Validation, Supervision, Resources, Project administration, Methodology, Funding acquisition, Conceptualization.

Funding

The authors gratefully acknowledge the financial support provided by IRSN (Institut de Radioprotection et de Sûreté Nucléaire/Institute for Radiation Protection and Nuclear Safety) and INSA Toulouse (Université de Toulouse). Additional funding from the European Joint Programme on Radioactive Waste (EURAD), specifically WP MAGIC, is also recognized.

Declaration of competing interest

The authors declare that they have no known competing financial interests or personal relationships that could have appeared to influence the work reported in this paper.

Appendix A. Supplementary data

Supplementary data to this article can be found online at https://doi.org/10.1016/j.cemconcomp.2026.106518.

Data availability

Data will be made available on request.

References

[1] M.I. Sánchez de Rojas, M.P. Luxán, M. Frías, N. García, The influence of different additions on portland cement hydration heat, Cement Concr. Res. 23 (1993) 46–54, https://doi.org/10.1016/0008-8846(93)90134-U.

[2] B.W. Langan, K. Weng, M.A. Ward, Effect of silica fume and fly ash on heat of hydration of Portland cement, Cement Concr. Res. 32 (2002) 1045–1051, https://doi.org/10.1016/S0008-8846(02)00742-1.

[3] L. Buffo-Lacarrière, A. Sellier, A. Turatsinze, G. Escadeillas, Finite element modelling of hardening concrete: application to the prediction of early age cracking for massive reinforced structures, Mater. Struct. 44 (2011) 1821–1835, https://doi.org/10.1617/s11527-011-9740-y.

[4] M. Juenger, J.L. Provis, J. Elsen, W. Matthes, R.D. Hooton, J. Duchesne, L. Courard, H. He, F. Michel, R. Snellings, N.D. Belie, Supplementary cementitious materials for concrete: characterization needs, MRS Online Proc. Libr. 1488 (2012), https://doi.org/10.1557/opl.2012.1536.

[5] M.D.A. Thomas, R.D. Hooton, A. Scott, H. Zibara, The effect of supplementary cementitious materials on chloride binding in hardened cement paste, Cement Concr. Res. 42 (2012) 1–7, https://doi.org/10.1016/j.cemconres.2011.01.001.

[6] K.-S. Lauch, V. Dieryck, V. Pollet, The Use of Ternary Cements to Reduce the Environmental Impact of Concrete, vol. 1, RILEM Technical Letters, 2016, pp. 88–93, https://doi.org/10.21809/rilemtechlett.2016.19.

[7] E. Sakai, S. Miyahara, S. Ohsawa, S.-H. Lee, M. Daimon, Hydration of fly ash cement, Cement Concr. Res. 35 (2005) 1135–1140, https://doi.org/10.1016/j.cemconres.2004.09.008.

[8] M. Codina, C. Cau-dit-Coumes, P. Le Bescop, J. Verdier, J.P. Ollivier, Design and characterization of low-heat and low-alkalinity cements, Cement Concr. Res. 38 (2008) 437–448, https://doi.org/10.1016/j.cemconres.2007.12.002.

[9] M.H. Shehata, M.D.A. Thomas, R.F. Bleszynski, The effects of fly ash composition on the chemistry of pore solution in hydrated cement pastes, Cement Concr. Res. 29 (1999) 1915–1920, https://doi.org/10.1016/S0008-8846(99)00190-8.

[10] B. Lothenbach, K. Scrivener, R.D. Hooton, Supplementary cementitious materials, Cement Concr. Res. 41 (2011) 1244–1256, https://doi.org/10.1016/j.cemconres.2010.12.001.

[11] M. Rosenqvist, A. Bertron, K. Fridh, M. Hassanzadeh, Concrete alteration due to 55years of exposure to river water: chemical and mineralogical characterisation, Cement Concr. Res. 92 (2017) 110–120, https://doi.org/10.1016/j.cemconres.2016.11.012.

[12] U.H. Jakobsen, K. De Weerdt, M.R. Geiker, Elemental zonation in marine concrete, Cement Concr. Res. 85 (2016) 12–27, https://doi.org/10.1016/j.cemconres.2016.02.006.

[13] A. Dauzères, P. Le Bescop, C. Cau-Dit-Coumes, F. Brunet, X. Bourbon, J. Timonen, M. Voutilainen, L. Chomat, P. Sardini, On the physico-chemical evolution of low-pH and CEM I cement pastes interacting with callovo-oxfordian pore water under its in situ CO2 partial pressure, Cement Concr. Res. 58 (2014) 76–88, https://doi.org/10.1016/j.cemconres.2014.01.010.

[14] A. Dauzeres, P. Le Bescop, P. Sardini, C. Cau Dit Coumes, Physico-chemical investigation of clayey/cement-based materials interaction in the context of geological waste disposal: experimental approach and results, Cement Concr. Res. 40 (2010) 1327–1340, https://doi.org/10.1016/j.cemconres.2010.03.015.

[15] E.C. Gaucher, P. Blanc, Cement/clay interactions – a review: experiments, natural analogues, and modeling, Waste Manag. 26 (2006) 776–788, https://doi.org/10.1016/j.wasman.2006.01.027.

[16] D. Savage, C. Walker, R. Arthur, C. Rochelle, C. Oda, H. Takase, Alteration of bentonite by hyperalkaline fluids: a review of the role of secondary minerals, Phys. Chem. Earth, Parts A/B/C 32 (2007) 287–297, https://doi.org/10.1016/j.pce.2005.08.048.

[17] U.H. Jakobsen, Microstructural surface deterioration of concrete exposed to seawater; results after 2 years exposure, 14th Euroseminar on Microscopy, Applied to Building Materials (2013) 10–14.

[18] A. Dauzeres, G. Achiedo, D. Nied, E. Bernard, S. Alahrache, B. Lothenbach, Magnesium perturbation in low-pH concretes placed in clayey environment—solid characterizations and modeling, Cement Concr. Res. 79 (2016) 137–150, https://doi.org/10.1016/j.cemconres.2015.09.002.

[19] C. Qiao, P. Suraneni, M. Tsui Chang, J. Weiss, Damage in cement pastes exposed to MgCl2 solutions, Mater. Struct. 51 (2018) 74, https://doi.org/10.1617/s11527-018-1191-2.

[20] J. Yang, D. Hou, Q. Ding, G. Zhang, Y. Zhang, H. Hu, Insight on the nanoscale chemical degradation mechanism of MgCl2 attack in cement paste, Constr. Build. Mater. 238 (2020) 117777, https://doi.org/10.1016/j.conbuildmat.2019.117777.

[21] A. Zhang, Y. Ge, G. Wang, Evaluating the use of nano-SiO2/Al2O3 to mitigate damage in cement mortar exposed to magnesium chloride solution under different conditions, Constr. Build. Mater. 392 (2023) 131965, https://doi.org/10.1016/j.conbuildmat.2023.131965.

[22] X. Liu, P. Feng, X. Yu, X. Shen, G. Geng, B. Lothenbach, The physiochemical alterations of calcium silicate hydrate (C-S-H) under magnesium attack, Cement Concr. Res. 160 (2022) 106901, https://doi.org/10.1016/j.cemconres.2022.106901.

[23] E. Bernard, B. Lothenbach, F. Le Goff, I. Pochard, A. Dauzères, Effect of magnesium on calcium silicate hydrate (C-S-H), Cement Concr. Res. 97 (2017) 61–72, https://doi.org/10.1016/j.cemconres.2017.03.012.

[24] C. Dewitte, L. Lacarrière, M. Neji, A. Bertron, A. Dauzères, Chemo-mechanical characterization of a low-pH model cement paste in magnesium bearing environment, Cement Concr. Res. 184 (2024) 107598, https://doi.org/10.1016/j.cemconres.2024.107598.

[25] S. Brunauer, P.H. Emmett, E. Teller, Adsorption of gases in multimolecular layers, J. Am. Chem. Soc. 60 (1938) 309–319, https://doi.org/10.1021/ja01269a023.

[26] E.P. Barrett, L.G. Joyner, P.P. Halenda, The determination of pore volume and area distributions in porous substances. I. Computations from nitrogen isotherms, J. Am. Chem. Soc. 73 (1951) 373–380, https://doi.org/10.1021/ja01145a126.

[27] A. Galarneau, D. Mehlhorn, F. Guenneau, B. Coasne, F. Villemot, D. Minoux, C. Aquino, J.-P. Dath, Specific surface area determination for microporous/mesoporous materials: the case of mesoporous FAU-Y zeolites, Langmuir 34 (2018) 14134–14142, https://doi.org/10.1021/acs.langmuir.8b02144.

[28] J.H. de Boer, B.C. Lippens, B.G. Linsen, J.C.P. Broekhoff, A. van den Heuvel, ThJ. Osinga, Thet-curve of multimolecular N2-adsorption, J. Colloid Interface Sci. 21 (1966) 405–414, https://doi.org/10.1016/0095-8522(66)90006-7.

[29] C. Dewitte, A. Bertron, M. Neji, L. Lacarrière, A. Dauzères, Chemical and microstructural properties of designed cohesive M-S-H pastes, Materials 15 (2022) 547, https://doi.org/10.3390/ma15020547.

[30] D.L. Nguyen, Nouvelle méthodologie d'identification des propriétés mécaniques locales d'un matériau hétérogène par nanoindentation : application aux matériaux du génie civil, thesis, Paris Est, http://www.theses.fr/2017PESC1028, 2017. (Accessed 1 April 2020).

[31] S.W. Swanton, T.G. Heath, A. Clacher, Leaching behaviour of low Ca:Si ratio CaO–SiO2–H2O systems, Cement Concr. Res. 88 (2016) 82–95, https://doi.org/10.1016/j.cemconres.2016.06.001.

[32] A.W. Harris, M.C. Manning, W.M. Tearle, C.J. Tweed, Testing of models of the dissolution of cements—leaching of synthetic CSH gels, Cement Concr. Res. 32 (2002) 731–746, https://doi.org/10.1016/S0008-8846(01)00748-7.

[33] C.S. Walker, S. Sutou, C. Oda, M. Mihara, A. Honda, Calcium silicate hydrate (C-S-H) gel solubility data and a discrete solid phase model at 25 °C based on two binary non-ideal solid solutions, Cement Concr. Res. 79 (2016) 1–30, https://doi.org/10.1016/j.cemconres.2015.07.006.

[34] P. Henocq, Modélisation Des Interactions Ioniques À La Surface Des Silicates De Calcium Hydratés, Cergy-Pontoise, 2005. These de doctorat, https://theses.fr/2005CERG0255. (Accessed 20 March 2024).

[35] D.A. Kulik, Improving the structural consistency of C-S-H solid solution thermodynamic models, Cement Concr. Res. 41 (2011) 477–495, https://doi.org/10.1016/j.cemconres.2011.01.012.

[36] C. Carde, J.-P. Ollivier, Caractérisation Et Modélisation De L'Altération Des Propriétés Mécaniques due À La Lixiviation Des Matériaux Cimentaires, 1996.

[37] C. Gallé, H. Peycelon, P. Le Bescop, Effect of an accelerated chemical degradation on water permeability and pore structure of cementbased materials, Adv. Cement Res. 16 (2004) 105–114, https://doi.org/10.1680/adcr.2004.16.3.105.

[38] G. Constantinides, F.-J. Ulm, The effect of two types of C-S-H on the elasticity of cement-based materials: results from nanoindentation and micromechanical modeling, Cement Concr. Res. 34 (2004) 67–80, https://doi.org/10.1016/S0008-8846(03)00230-8.

[39] E. Stora, B. Bary, Q.-C. He, E. Deville, P. Montarnal, Modelling and simulations of the chemo–mechanical behaviour of leached cement-based materials: leaching process and induced loss of stiffness, Cement Concr. Res. 39 (2009) 763–772, https://doi.org/10.1016/j.cemconres.2009.05.010.